

Quantum dot infrared photodetector enhanced by surface plasma wave excitation

S. C. Lee, S. Krishna, and S. R. J. Brueck,*

Center for High Technology Materials and Department of Electrical and Computer Engineering, University of New Mexico, 1313 Goddard SE, Albuquerque, NM 87106
*sclee@chtm.unm.edu

Abstract: Up to a thirty-fold detectivity enhancement is achieved for an InAs quantum dot infrared photodetector (QDIP) by the excitation of surface plasma waves (SPWs) using a metal photonic crystal (MPC) integrated on top of the detector absorption region. The MPC is a 100 nm-thick gold film perforated with a 3.6 μm period square array of circular holes. A bare QDIP shows a bias-tunable broadband response from ~ 6 to 10 μm associated with the quantum confined Stark (QCS) effect. On the other hand, an MPC-integrated QDIP exhibits a dominant peak at 11.3 μm with a ~ 1 μm full width at half maximum and the highly enhanced detectivity at the bias polarity optimized for long wavelength. This is very different from the photoresponse of the bare QDIP but fully consistent with the direct coupling of the QDs in the detector absorption region to the SPWs excited at the MPC/detector interface by incident photons. The SPW resonance wavelength, λ , for the smallest coupling wavevector of the array in the MPC is close to 11.3 μm . The response also shows other SPW-coupled peaks: a significant peak at 8.1 μm ($\sim\lambda/\sqrt{2}$) and noticeable peaks at 5.8 μm ($\sim\lambda/2$) and 5.4 μm ($\sim\lambda/\sqrt{5}$) which correspond to higher-order coupling wavevectors. For the opposite bias, the MPC-integrated QDIP shows the highest response at 8.1 μm , providing a dramatic voltage tunability that is associated with QCS effect. SPWs propagate with TM (x, z) polarization along the MPC/detector interface. The enhanced detectivity is explained by these characteristics which increase both the effective absorption cross section with propagation and the interaction strength with TM polarization in the coupling to the QDs. Simulations show good qualitative agreement with the observed spectral behavior.

©2009 Optical Society of America

OCIS codes: (130.3060) Infrared; (230.5160) Photodetectors; (240.6680) Surface plasmons; (250.5403) Plasmonics; (310.6628) Subwavelength structures, nanostructures.

References and links

1. For a recent review see, C. Genet, and T. W. Ebbesen, "Light in tiny holes," *Nature* **445**(7123), 39–46 (2007).
2. E. Cubukcu, E. A. Kort, K. B. Crozier, and F. Capasso, "Plasmonic laser antenna," *Appl. Phys. Lett.* **89**(9), 093120 (2006).
3. R. F. Oulton, V. J. Sorger, T. Zentgraf, R.-M. Ma, C. Gladden, L. Dai, G. Bartal, and X. Zhang, "Plasmon lasers at deep subwavelength scale," *Nature* **461**(7264), 629–632 (2009).
4. S. R. J. Brueck, V. Diadiuk, T. Jones, and W. Lenth, "Enhanced quantum efficiency internal photoemission detectors by grating coupling to surface plasma waves," *Appl. Phys. Lett.* **46**(10), 915–917 (1985).
5. A. Sellai, and P. Dawson, "Quantum efficiency in GaAs Schottky photodetectors with enhancement due to surface plasmon excitations," *Solid-State Electron.* **46**(1), 29–33 (2002).
6. Z. Yu, G. Veronis, S. Fan, and M. L. Brongersma, "Design of midinfrared photodetectors enhanced by surface plasmons on grating structures," *Appl. Phys. Lett.* **89**(15), 151116 (2006).
7. S. C. Lee, E. Plis, S. Krishna, and S. R. J. Brueck, "Mid-infrared transmission enhancement through sub-wavelength metal hole array using impedance-matching dielectric layer," *Electron. Lett.* **45**(12), 643–645 (2009).

8. D. Okamoto, J. Fijikata, K. Nishi, and K. Ohashi, "Numerical studies of near-infrared photodetectors with surface plasmon antennas for optical communications," *Jpn. J. Appl. Phys.* **47**(4), 2921–2923 (2008).
9. G. Vane, and A. F. H. Goetz, "Terrestrial imaging spectroscopy," *Remote Sens. Environ.* **24**(1), 1–29 (1988).
10. J. P. Kerekes, M. K. Griffin, J. E. Baum, and K. E. Farrar, "Modeling of LWIR hyperspectral system performance for surface object and effluent detection applications," *Proc. SPIE* **4381**, 348–359 (2001).
11. D. Manolakis, and G. A. Shaw, "Detection algorithms for hyperspectral imaging applications," *IEEE Signal Process. Mag.* **19**(1), 29–43 (2002).
12. A. C. Goldberg, T. Fischer, and Z. I. Derzko, "Application of dual band infrared focal plane arrays to tactical and strategic military problems," *Proc. SPIE* **4480**, 500–514 (2002).
13. E. P. G. Smith, E. A. Patten, P. M. Goetz, G. M. Venzor, J. A. Roth, B. Z. Nosh, J. D. Benson, A. J. Stoltz, J. B. Varesi, J. E. Jensen, S. M. Johnson, and W. A. Radford, "Fabrication and Characterization of Two-Color Midwavelength/Long Wavelength HgCdTe Infrared Detectors," *J. Electron. Mater.* **35**(6), 1145–1152 (2006).
14. W. R. Bell, "MTI: overview," *Proc. SPIE* **4381**, 173–183 (2001)
15. H. Raether, *Surface Plasmons* (Springer, 1988), p5–6.
16. R. Qiang, R. L. Chen, and J. Chen, "Modeling electrical properties of fold films at infrared frequency using FDTD method," *Int. J. Infrared Millim. Waves* **25**(8), 1263–1270 (2004).
17. S. Krishna, S. Raghavan, G. von Winckel, A. Stintz, G. Ariyawansa, S. G. Matsik, and A. G. U. Perera, "Three-color ($\lambda_{p1} \sim 3.8 \mu\text{m}$, $\lambda_{p2} \sim 8.5 \mu\text{m}$ and $\lambda_{p3} \sim 23.2 \mu\text{m}$) InAs/InGaAs quantum-dots-in-a-well detector," *Appl. Phys. Lett.* **83**(14), 2745–2747 (2003).
18. S. Krishna, D. Forman, S. Annamalai, P. Dowd, P. Varangis, T. Tumolillo, A. Gray, J. Zilko, K. Sun, M. Liu, J. Campbell, and D. Carothers, "Demonstration of a 320 x 256 Two-Color Focal Plane Array Using InAs/InGaAs Quantum Dots in a Well Detectors," *Appl. Phys. Lett.* **86**(19), 193501 (2005).
19. E. L. Dereniak and G. D. Boreman, *Infrared detectors and systems* (Wiley 1996), p208.
20. These values are lower than previously reported data. This is partly because the crosstalk between neighbor devices and the extra absorption by residual IR have been minimized for precise comparison between the two devices.
21. B. K. Minhas, W. Fan, K. Agi, S. R. J. Brueck, and K. J. Malloy, "Metallic inductive and capacitive grids: theory and experiment," *J. Opt. Soc. Am. A* **19**(7), 1352–1259 (2002).
22. In RCWA, the propagation length, and the transverse penetration depth below, the dielectric constant of gold was calculated from a Drude model with bulk plasma and scattering frequencies [Ordal *et al.*, *Appl. Opt.* **22**, 1099 (1983)]. The low-temperature refractive index of GaAs ~ 3.2 for the wavelengths of interest in this work was taken for ϵ'_d of the QDIP material [J. S. Blakemore, *J. Appl. Phys.* **62**, 4528 (1987)].
23. S. J. Chua, S. J. Xu, X. H. Zhang, X. C. Wang, T. Mei, W. J. Fan, C. H. Wang, J. Jiang, and X. G. Xie, "Polarization dependence of intraband absorption in self-organized quantum dots," *Appl. Phys. Lett.* **73**(14), 1997–1999 (1998).
24. S. Sauvage, P. Boucaud, T. Brunhes, V. Immer, E. Finkman, and J.-M. Gerard, "Midinfrared absorption and photocurrent spectroscopy of InAs/GaAs self-assembled quantum dots," *Appl. Phys. Lett.* **78**(16), 2327–2329 (2001).

1. Introduction

Recently, the optical properties of a thin metal film perforated by 2-dimensional (2D) hole arrays, a metal photonic crystal (MPC), and the role of surface plasma waves (SPWs) in the extraordinary optical transmission of this MPC have been studied extensively [1]. The SPW is bound to the metal/dielectric interface with an evanescent field that decays exponentially away from the interface. Resonances are observed when a wavevector of the array provides phase-matching between the incident photon and SPWs at either of the metal/dielectric interfaces. These interactions can be used to improve the performance of both optical emitters [2, 3] and detectors [4–8]. SPW-coupled detectors are expected to have a significant impact on infrared spectral imagery, which is increasingly important for many remote sensing problems including defeating camouflage [9], remote identification of chemical and biological compounds [10], and anomaly detection [11]. Such spectral imagery can take on many forms: two-color infrared imagery useful for applications such as locating recently disturbed earth [12, 13]; multispectral imagery where a small number of bands (usually 3 – 15) are spread out across the total spectrum [14]; or hyperspectral imagery where a detailed spectral measurement is made at every pixel of a focal plane array (FPA) [9].

In this work, we probe the direct coupling of the SPW excited at the MPC/detector interface through its contribution to the photoresponse of a quantum dot infrared photodetector (QDIP) with an absorption region located within the transverse extent of the SPW. A dramatic, $30\times$ increase in the photoresponse is found at the resonance wavelength of

the SPW coupling. The SPW response interacting with the quantum confined Stark (QCS) effect in the quantum dots (QDs) provides a unique spectral response tuning mechanism that offers a new and powerful, fully integrated approach to spectral sensitivity variation that is easily adaptable to large FPAs.

2. MPC design

Figure 1 shows an optical microscope image of an MPC-integrated device (a) along with a schematic cross sectional view of the sample structure (b). The MPC is a 100 nm-thick Au film perforated with a 3.6 μm period square array of circular holes having diameter of $1.65 \pm 0.05 \mu\text{m}$. For a gold MPC having a hole period, p , integrated on a QDIP grown on a GaAs substrate, the SPW resonance wavelengths, λ_{ij} , at the MPC/detector interface, are given as [15]:

$$\lambda_{ij} = \frac{p}{\sqrt{i^2 + j^2}} \operatorname{Re} \left\{ \left[\frac{\epsilon_m \epsilon_d}{\epsilon_m + \epsilon_d} \right]^{1/2} \right\}, \quad (1)$$

where the integers, i and j , correspond to the orders of the 2D grating wavevector in the orthogonal spatial directions; $\epsilon_d = \epsilon_d' + i\epsilon_d''$ and $\epsilon_m = \epsilon_m' + i\epsilon_m''$ are the dielectric constants of the QDIP material (including the intraband absorption) and the Au film at a given resonance wavelength [1]. The thickness of the MPC used in this work is considerably greater than the metal skin depth to avoid direct transmission [16]. For convenience, λ_{01} ($= \lambda_{10}$), λ_{11} , λ_{02} ($= \lambda_{20}$), and λ_{12} ($= \lambda_{21}$) are referred to as the resonance wavelengths of the SPWs excited at MPC/detector interface. For normal incidence, these resonance wavelengths are approximately given by: $\lambda_{10} \sim n_d p$, $\lambda_{11} \sim \lambda_{10}/\sqrt{2}$, $\lambda_{02} \sim \lambda_{10}/2$, and $\lambda_{12} \sim \lambda_{10}/\sqrt{5}$, where $n_d = \sqrt{\epsilon_d'}$. As seen below, the period of 3.6 μm was chosen to align the fundamental resonance (λ_{10}) with the long wavelength edge of the QDIP response so that there would be a large response variation associated with the QCS bias dependence.

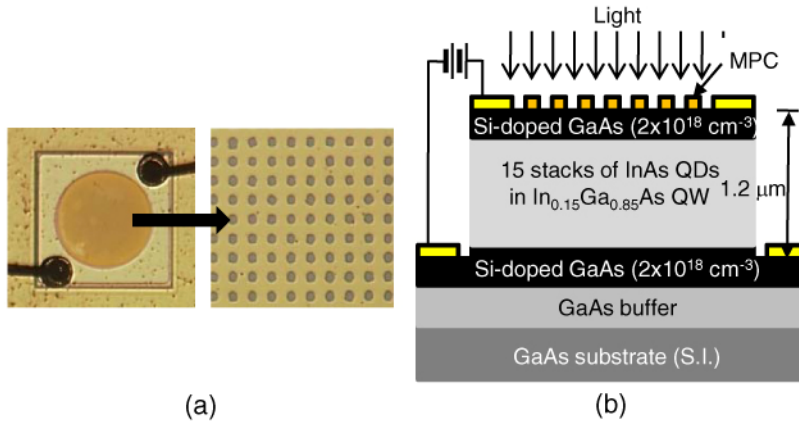


Fig. 1. (a) Optical microscope images of the MPC device (left) and with 16 \times higher magnification revealing the details of the MPC (right). The period of the circular holes is 3.6 μm . (b) A schematic cross sectional structure of the MPC device.

3. QDIP growth and device fabrication

The QDIP was grown on a semi-insulating GaAs(001) substrate by molecular beam epitaxy. As shown in Fig. 1(b), the MPC is integrated atop a QDIP with an absorption region consisting of 15 stacks of InAs QDs. Each QD stack buried in a undoped 11 nm-thick $\text{In}_{0.15}\text{Ga}_{0.85}\text{As}$ quantum well (QW) has a dot density of $\sim 3 \times 10^{10} \text{ cm}^{-2}$. For this structure, the ground state of the InAs QD relative to the conduction band of GaAs is approximately 250

meV [17]. The total thickness of the absorption region is 980 nm. A 10 nm-thick Cr film was deposited between the MPC and the QDIP to promote the adhesion of the Au film to the top GaAs layer. The device mesa size is $410 \times 410 \mu\text{m}^2$ and the diameter of the detector aperture or the lateral dimension of the MPC is $300 \mu\text{m}$. The vertical distance from the MPC/detector interface to the end of the absorption region is $1.2 \mu\text{m}$. Figure 1(b) schematically shows a diagram with positive bias to the top contact at the MPC (This is arbitrarily referred to below as forward bias.).

This MPC-integrated QDIP (MPC device) is compared with a reference QDIP without an MPC (reference device). Both devices were taken from a single die of the same wafer and therefore their intrinsic response and performance are assumed to be very similar. Standard photolithography and electron-beam metal deposition were employed for the fabrication of these devices and the MPC.

4. Results

The low temperature photoresponse (10K) was measured using a Nicolet 6700 Fourier transform infrared spectrometer and a Stanford Research Systems SR FFT 770 network analyzer. The bias applied to the devices was varied from -5 to 5 V.

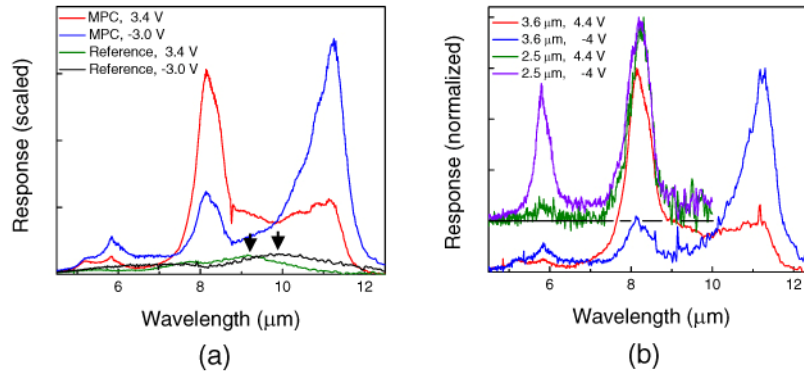


Fig. 2. (a) Spectral response curves of the reference device (two spectra at the bottom with the arrows indicating the highest peak in each spectrum) and the MPC device (other two spectra with higher responsivity) for -3.0 V and 3.4 V at 10 K. (b) Spectral response curves of the 3.6 and $2.5 \mu\text{m}$ -period MPC devices for -4.0 V and 4.4 V at 10 K. Each spectrum was normalized by its highest peak intensity. Note that the spectra of the shorter period MPC device are offset for clarity.

Figure 2(a) shows the spectral response of the MPC and reference devices at -3.0 and 3.4 V, respectively. As indicated by the arrows in the figure, the reference device exhibits two rather broad and indistinct peaks for both -3.0 V (the strongest at $9.9 \mu\text{m}$ and a second at $7.3 \mu\text{m}$), and 3.4 V (the strongest at $9.2 \mu\text{m}$ and a second at $5.5 \mu\text{m}$). This two color response agrees with previously reported data [18]. The peak shifts with applied voltage have been interpreted as a QCS effect [18]. On the other hand, the MPC device has four peaks at identical wavelengths but varying responsivity for both biases. The peak at $11.3 \mu\text{m}$, which is much stronger than that of the reference device, is dominant for reverse bias while the peak at $8.1 \mu\text{m}$ is more intense than any other peaks for forward bias. The two remaining peaks at 5.8 and $5.4 \mu\text{m}$ are relatively weak. In Fig. 2(a), therefore, the MPC device has totally different voltage dependent spectral responsivity from the reference device in both peak wavelength and especially response intensity.

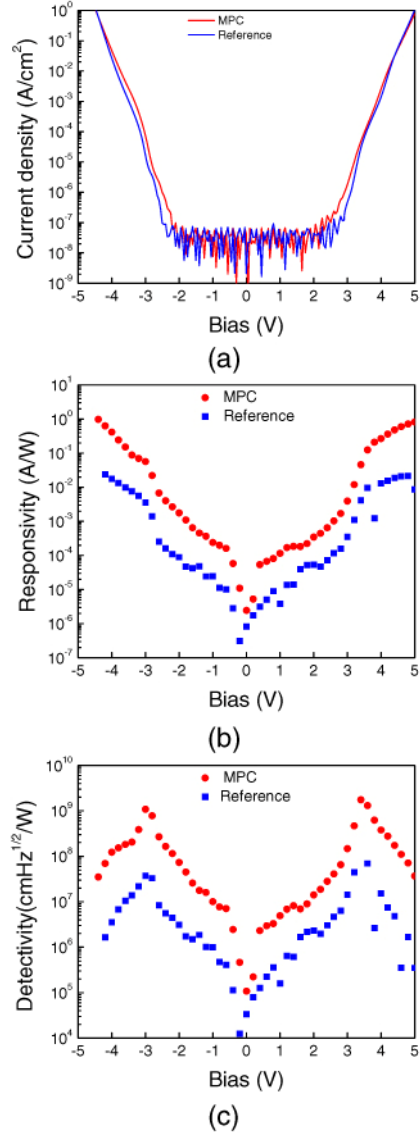


Fig. 3. (a) I-V characteristics, (b) responsivity, and (c) detectivity of the 3.6 μm -period MPC and the reference device at 10K.

Figure 3(a) presents the I-V characteristics of two devices, where the MPC device exhibits a somewhat higher background current density than the reference device at the same bias. The current density of the MPC device at -3V is, for example, $7.2 \times 10^{-5} \text{ A/cm}^2$, greater than $1.6 \times 10^{-5} \text{ A/cm}^2$ of the reference device at the same bias. The flat region between -2.0 and 2.5 V is the noise floor of our instrumentation.

Figure 3(b) and 3(c) are the plots of the responsivity and detectivity of the two devices versus bias. They were measured by an 800 K black body source with 800 Hz frequency chopping and the noise signal from a 293 K background with $f/1$ optics. As seen in Fig. 3(c), each device has a maximum detectivity at -3.0 V and 3.4 V , referred to as the peak voltages, V_p 's. In Figs. 3(b) and (c), the responsivity and detectivity of the reference device are slightly asymmetric with respect to zero bias. They are 0.014 and 0.016 A/W and 1.5×10^8 and $3.7 \times 10^8 \text{ cmHz}^{1/2}/\text{W}$ at reverse and forward V_p , respectively [19,20]. On the other hand, these

parameters are larger by over an order of magnitude for the MPC device. Also, this device has an asymmetric dependence on bias, as observed in Figs. 3(b) and 3(c). The responsivities of the MPC device at reverse and forward V_b correspond to 0.23 and 0.18 A/W. The highest detectivities of the MPC device are 4.4×10^9 and 7.2×10^9 cmHz^{1/2}/W for reverse and forward V_p respectively. For these biases, the detectivity ratios of the MPC to the reference device are 29 (reverse V_p) and 19 (forward V_p). This is a remarkable enhancement in detectivity. For a bias higher than the turn-on voltage $\sim \pm 2$ V, the detectivity ratio roughly ranges from 20 to 30. The slight asymmetric I-V of Fig. 2(a) which is partly due to the asymmetric 3-dimensional shape of the QDs is reflected in the responsivity and as a result in the lower detectivity ratio (= 19) of the MPC device for forward bias. The measured data are summarized in Table 1.

Table 1 Summary of measurement and modeling.

	Bias (V)	Device	λ_{01} (μm)	λ_{11} (μm)	λ_{02} (μm)	λ_{12} (μm)	Responsivity (A/W)	Detectivity ($\times 10^9$ cmHz ^{1/2} /W)
Experiment	-3.0	MPC	11.3	8.1	5.8	5.4	0.23	4.4
		Reference	Highest at 9.9 μm				0.014	0.15
	3.4	MPC	11.3	8.1	5.8	5.4	0.18	7.2
		Reference	Highest at 9.2 μm				0.016	0.37
Theory (μm)	λ_{ij} from RCWA		11.7	8.3	5.7	5.3		
	δ_{sp} at λ_{ij}		14.1	7.2	3.7	3.2		
	L_{sp} at λ_{ij} with QD absorption	none	1470	740	380	330		
		2%	27.5 \pm 0.5					
		10%	5.1					

5. Discussion

As shown in Fig. 4(a), the resonance wavelengths of Eq. (1) associated with the MPC/detector interface are identified from the normal-incidence spectral absorption (= 1 - R - T, where R and T are reflection and transmission respectively), simulated by rigorous coupled wave analysis (RCWA) [21]. They are 11.7, 8.3, 5.7, 5.3 μm for λ_{01} , λ_{11} , λ_{02} , and λ_{12} , respectively [22]. Both calculated and measured λ_{ij} 's are summarized in Table 1. Together with the spectral response from the MPC device examined earlier, Fig. 2(b) also presents the responses for the two bias polarities from the same type QDIP but integrated with an MPC having a shorter period of 2.5 μm . The resulting device consistently has a similar enhanced performance. Because of the shorter period, the resonance wavelengths calculated from RCWA shift to $\lambda_{01} = 8.3$ and $\lambda_{11} = 5.6$ μm . As seen in Fig. 2(b), the measurements from this device coincide with these calculated wavelengths and support the peak identifications shown in Fig. 4(a).

If the enhancement of the photoresponse of the MPC device shown in Fig. 2(a) is caused by the direct coupling of the QDs in the detector absorption region to SPW excitation at those resonance wavelengths (SPW-QD coupling), the strength of the evanescent field associated with the SPWs at the MPC/detector interface should be correlated to the enhanced detectivity. Then, the photoresponse of the MPC device coupled to this field can be estimated from that of the reference device weighted by the calculated absorption in Fig. 4(a). The results of this evaluation are shown in Fig. 4(b). The actual measurement is taken at $\sim f/4$, and the variation in the angle of incidence will broaden the response from the very narrow peaks calculated for normal incidence. As mentioned above, the peak shift in the photoresponse of a QDIP with bias polarity has been explained by the QCS effect. However, the resonance wavelengths of the SPWs excited at MPC/detector interface are not affected by the bias. This is consistent with Fig. 2(a) and Table 1; the resonance wavelengths are independent of bias polarity. On the contrary, the original photoresponse of a QDIP does vary with voltage because of the QCS effect, explaining the different coupling strength at the same λ_{ij} as the polarity of the bias is changed. The absorption-weighted photoresponse of the reference device shown in Fig.

4(b) reveals peak intensities consistent with the experimental results shown in Fig. 2(a). Except for line broadening, the theoretical photoresponse agrees with the experimental data in both resonance wavelength and corresponding relative intensity for given biases, as seen in Figs. 2(a), 4(b), and Table 1.

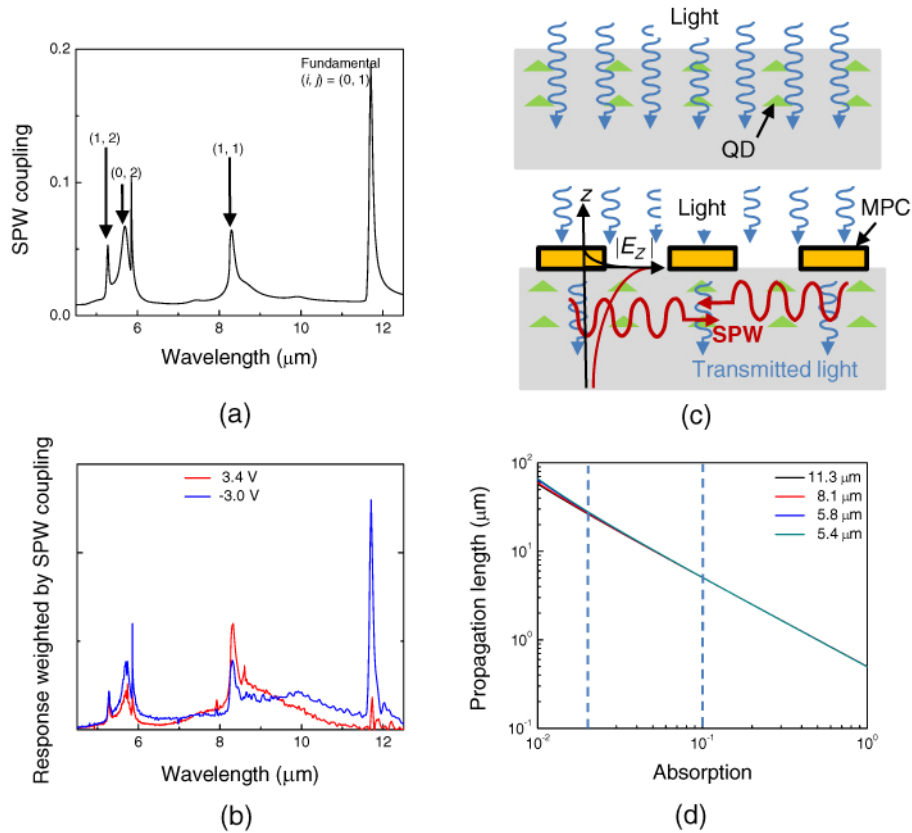


Fig. 4. (a) Calculated normal-incidence absorption spectrum ($= 1 - R - T$ with reflection, R , and transmission, T) from a RCWA simulation for the MPC. (b) Spectral response curves of the reference device in Fig. 2(a) weighted by the SPW coupling from the RCWA simulation in (a). See the text for details. (c) A schematic illustration for the model proposed in this work (not scaled). The top illustration is the cross section view of a QDIP with no MPC and the bottom is that of the same QDIP with an MPC. Only two QD stacks are shown for clarity. (d) A plot of propagation length (L_{sp}) as a function of the QD absorption. The four wavelengths in this plot correspond to the SPW resonance wavelengths in Table 1. The two vertical dashed lines indicate $\sim 2\%$ (left) absorption (measured for a single transit through the active region) and the $5 \times$ enhanced absorption (right) estimated for TM polarization. See the text for details.

As summarized in Table 1, both responsivity and detectivity are dramatically enhanced by the integration of an MPC on a QDIP. The physics leading to this observation is schematically illustrated in Fig. 4(c). SPWs propagate along the MPC/detector interface with a propagation length, L_{sp} . Then, the absorption cross section of the QDs can be effectively increased by SPW propagation. Also, SPWs include an electric-field polarization component normal to the interface (E_z -directed). In contrast, for the reference device, incident photons propagate normal to the QD stacks and across only the 980 nm-thick absorption region of Fig. 1(b) with a polarization parallel to the top surface (e. g. E_x -directed). Similar to the polarization dependence of QW absorption, the E_z -directed field is more efficient than the E_x -directed field in interacting with the QDs of Fig. 4(c) [23,24]. The photoresponse of the MPC

device is enhanced as a result of the propagation and E_z -directed field (TM-polarization) of SPWs.

The measured, normal-incidence absorption through a bare QDIP material of Fig. 1(b) is roughly 2% around 10 μm . This QD absorption must be considered in L_{sp} and the transverse penetration depth into the detector of the evanescent field associated with SPWs, δ_{sp} , since, as seen below, the detector absorption region is within δ_{sp} from the MPC/detector interface. These lengths can be easily derived by expanding the well-known expressions of the wavevector at a *unpatterned* metal/dielectric interface, $k_x^{\text{sp}} = 2\pi/\lambda \sqrt{\epsilon_m \epsilon_d / (\epsilon_m + \epsilon_d)}$, and $k_z^{\text{sp}} = 2\pi/\lambda \sqrt{-\epsilon_d^2 / (\epsilon_m + \epsilon_d)}$ under the assumptions $|\epsilon_m'| \gg \epsilon_d'$, ϵ_m'' and $\epsilon_d' \gg \epsilon_d''$ [15,22]:

$$L_{\text{sp}} \sim \frac{\lambda}{\pi} \frac{1}{\frac{\epsilon_d''}{\epsilon_d'} \left(1 - \frac{\epsilon_d'}{\epsilon_m'}\right) + \frac{\epsilon_m'' \epsilon_d'}{(\epsilon_m')^2}} \quad \text{and} \quad \delta_{\text{sp}} \sim \frac{\lambda}{2\pi} \sqrt{\frac{\epsilon_m' + \epsilon_d'}{-\epsilon_d'^2}}. \quad (2)$$

Here, λ is wavelength and corresponds to λ_{ij} of Eq. (1) at each SPW mode. The resonance wavelengths are not strongly dependent on the loss for $\epsilon_d'' \ll \epsilon_d'$. As seen in Eq. (2), δ_{sp} is independent of ϵ_d'' and ϵ_m'' to the lowest order. However, L_{sp} is affected by the loss in both the metal and the dielectric. Figure 4(d) presents the L_{sp} of Eq. (2), estimated for an Au/GaAs interface at the wavelengths of interest in this work, as a function of absorption which includes the loss in the QD stacks under the interface. In this figure, L_{sp} decreases with increasing absorption by the QD stacks and becomes $\sim 30 \mu\text{m}$ at 2% absorption. Without the QD absorption, L_{sp} is $\sim 1 \text{ mm}$ at these wavelengths. This implies that the QD absorption dominates in SPW propagation compared with the impact of the metal absorption. The L_{sp} 's and δ_{sp} 's at all λ_{ij} 's calculated from Eq. (2) under these conditions are summarized in Table 1. While δ_{sp} depends on λ_{ij} , L_{sp} is almost independent of it. For all of the wavelengths of interest, δ_{sp} in Table 1 is larger than the thickness of the detector absorption region ($\sim 1 \mu\text{m}$), so that the SPWs effectively interact with the entire QD stacks shown in Fig. 1(b). In Fig. 4(d) and Table 1, L_{sp} is dominated by the QDIP absorption and is not in the mm range as it would be for a lossless dielectric but is still considerably greater than the thickness of the absorption region. Thus, an estimate of $\sim 5 \times$ enhanced interaction strength of the QDs with the TM-polarized SPWs [23, 24] and the increased effective absorption cross section of the QDs by propagating SPWs with $L_{\text{sp}} \sim 5 - 30 \mu\text{m}$ along the MPC/detector interface can explain the dramatic enhancement of the QDIP performance with the integration of an MPC. The actual change of the interaction strength with polarization varies with the details of the QD structure. The optical properties of an MPC are essentially independent of temperature. The results of the SPW-QD coupling would be similar for higher temperature operation, allowing for the bandgap shifts and increased noise of a QDIP with temperature.

The RCWA simulation provides the SPW excitation for an ideal MPC structure. A small variation of parameters such as the diameter and the precise shape of each hole results in relatively weak, multiple absorption peaks associated in particular with the higher energy resonances, e.g. for wavelengths shorter than λ_{11} . These could be localized SPWs, associated with individual holes. In the experiment, however, these features are not resolved as a result of inhomogeneity of the sample structure, for example, hole diameter fluctuation, and experimental inhomogeneity associated with the range of incident angles in the experiment. A good example of such a feature is the sharp spike on the right of the SPW at λ_{12} in Fig. 4(a) which is absent in the measurement of Fig. 2(a). Further study is required for better understanding of the enhancement mechanism observed from a QDIP integrated with an MPC.

As seen in Figs. 2(a) and 2(b), the bias-dependent responsivity produces a dramatic change in the spectral photoresponse of the MPC device when it is convolved with the SPW

resonances. For the 2.5 μm -period device of Fig. 2(b), the photoresponse at λ_{01} is dominant for forward bias and comparable to that at λ_{11} for reverse bias, unlike the 3.6 μm -period MPC device. This can be also explained by the interaction of the SPW resonances with QCS effect and pattern shape. In reverse bias, the device functions as a narrow band ($< 1 \mu\text{m}$), two-color photodetector with a clear extension of working wavelength to $\sim 5 \mu\text{m}$. Depending on the period of the MPC, therefore, multi-color detection over the wide wavelength span is available by the integration of an MPC on a QDIP. Furthermore, a great deal of flexibility in the spectral and polarization response will be possible with additional subtlety in the design of the MPC. This provides entirely new degrees of freedom in designing individual detectors and FPAs.

Generally, the dots-in-a-well photodetector shown in Fig. 1 has a multi-color response since there are several absorption mechanisms: intersubband within a dot, dot-to-well and dot-to-continuum. In addition, the QCS effect provides tunability within these bands. An MPC-integrated QDIP adds yet another adjustable, and polarization-dependent, spectral selection mechanism. The interaction between the SPW resonances and the QCS tuning allows various spectral responses for a given detector. By choosing the spatial period to locate the two lowest order SPW resonance wavelengths, λ_{01} and λ_{11} , on opposite sides of the dominant photoresponse peak, as seen in Fig. 2(a), the MPC can provide widely tunable functionality to a QDIP with a switch for color selection by reversing the bias. Additional flexibility is possible with multiple array periods (Moiré patterns), and by adjusting the shapes of the individual features (for example slits rather than the simple holes in this first demonstration) offering the possibility of fully customizable wavelength and polarization response.

6. Conclusion

A dramatic thirtyfold detectivity enhancement by the direct coupling of SPWs to QDs has been demonstrated in an InAs QDIP with the integration of an MPC. A 100-nm-thick gold MPC perforated with a 3.6- μm -period square array of circular holes couples to SPWs at 11.3 and 8.1 μm where the MPC-integrated QDIP exhibits the strongest detectivity peak for reverse and forward bias respectively. A model based on the SPW propagation parallel to the MPC/detector interface is proposed to explain this extraordinary enhancement. SPWs propagate along the MPC/detector interface parallel to the QD stacks, with a TM-polarized (x , z) evanescent field extending into the detector absorption region. This increases both the interaction length compared with a single transit across a QDIP, and the absorption strength as a result of the polarization dependence of the QDs which favors z -directed electric fields. This SPW-QD coupling by the MPC integration contributes to the photocurrent providing a significantly enhanced detectivity and ultimately leads to high performance, spectrally selective QDIPs.

Acknowledgments

This work was partially supported by the Air Force Office of Scientific Research and by AFRL grant #433206 FA9453-07-C-0171.